



Reaction intermediates during operando electrocatalysis identified from full solvent quantum mechanics molecular dynamics

Tao Cheng^{a,b,c}, Alessandro Fortunelli^{c,d}, and William A. Goddard III^{b,c,1}

^aInstitute of Functional Nano & Soft Materials (FUNSOM), Jiangsu Key Laboratory for Carbon-Based Functional Materials & Devices, Joint International Research Laboratory of Carbon-Based Functional Materials and Devices, Soochow University, Suzhou, 215123, Jiangsu, PR China; ^bJoint Center for Artificial Photosynthesis, California Institute of Technology, Pasadena, CA 91125; ^cMaterials and Process Simulation Center, California Institute of Technology, Pasadena, CA 91125; and ^dItalian National Council for Research-Institute for the Chemistry of OrganoMetallic Compounds, Consiglio Nazionale delle Ricerche, Pisa 56124, Italy

Contributed by William A. Goddard III, January 28, 2019 (sent for review December 20, 2018; reviewed by Sharon Hammes-Schiffer, Philippe Sautet, and Richard J. Saykally)

Electrocatalysis provides a powerful means to selectively transform molecules, but a serious impediment in making rapid progress is the lack of a molecular-based understanding of the reactive mechanisms or intermediates at the electrode–electrolyte interface (EEI). Recent experimental techniques have been developed for operando identification of reaction intermediates using surface infrared (IR) and Raman spectroscopy. However, large noises in the experimental spectrum pose great challenges in resolving the atomistic structures of reactive intermediates. To provide an interpretation of these experimental studies and target for additional studies, we report the results from quantum mechanics molecular dynamics (QM-MD) with explicit consideration of solvent, electrode–electrolyte interface, and applied potential at 298 K, which conceptually resemble the operando experimental condition, leading to a prototype of operando QM-MD (o-QM-MD). With o-QM-MD, we characterize 22 possible reactive intermediates in carbon dioxide reduction reactions (CO₂RRs). Furthermore, we report the vibrational density of states (v-DoSs) of these intermediates from two-phase thermodynamic (2PT) analysis. Accordingly, we identify important intermediates such as chemisorbed CO₂ (*b*-CO₂), *HOC-COH, *C-CH, and *C-COH in our o-QM-MD likely to explain the experimental spectrum. Indeed, we assign the experimental peak at 1,191 cm⁻¹ to the mode of C-O stretch in *HOC-COH predicted at 1,189 cm⁻¹ and the experimental peak at 1,584 cm⁻¹ to the mode of C-C stretch in *C-COD predicted at 1,581 cm⁻¹. Interestingly, we find that surface ketene (*C=C=O), arising from *HOC-COH dehydration, also shows signals at around 1,584 cm⁻¹, which indicates a nonelectrochemical pathway of hydrocarbon formation at low overpotential and high pH conditions.

quantum mechanics | molecular dynamics | vibration mode | CO₂ reduction reaction | reaction mechanism

Electrocatalytic reactions play a key role in many modern and emerging critical technologies such as energy conversion and storage, sensors, organic synthesis, and biomolecular electronics. However, with very few exceptions, a fundamental understanding of electrocatalytic reactions remains poor and nonpredictive. This is because electrocatalytic reactions are extremely complex. The factors determining reaction pathways depend on the relative rates of the several competing intermediate steps. Moreover, these reactions take place in a strong electric field of the electric double layer (EDL). Along with the structure of the catalyst surface, the structure of the EDL controls the thermodynamics and kinetics of the elementary steps through the polarization and local microenvironment of the adsorbed species, interfacial charge transfer, and mass transfer to/from the catalytic site. These critical phenomena must be understood at the atomistic level to use them in developing new strategies for improving the efficiency of electrocatalytic processes. This makes atomistic

molecular-level understanding of electrocatalytic reactions is a scientific grand challenge.

Current understanding of electrode–electrolyte interfaces (EEIs) generally rests on continuum concepts of the EDL developed by Gouy, Chapman, Stern, and others. These theoretical models address the structural and electrical organization of the EDL, but have not been connected to the detailed atomistic description of reactions and electron/proton transfer at the molecular level of quantum mechanics (QM), nor have they been adequately validated experimentally due to the limitations of available techniques.

To provide an atomistic-level understanding of the nature of the EEI during electrocatalytic reactions (or operando), we have been using metadynamics reactive dynamics with QM-based forces to determine the free-energy barriers and onset potentials at 298 K, which we have applied to the carbon dioxide (CO₂) reduction reaction (CO₂RR). We use these results to elucidate the details of atom/charge flow and chemical transformations, electron/proton transfer, and ion transfer, and how they depend on applied potential (*U*). We expect that this will dramatically accelerate the development of electrocatalysis-based technologies.

CO₂RR has been studied extensively because of its central role in closing the carbon loop (1, 2). Electrocatalytically

Significance

The gap preventing a direct comparison between experiment and atomic simulation still exists due to the unrealistic consideration of the operando experimental condition in commonly used quantum mechanics (QM). In this work, we advanced the QM-based simulation of the electrode–electrolyte interface with explicit consideration of solvent and applied voltage to produce reactive trajectories as input for a two-phase thermodynamics model in generating vibrational density of states that can be directly compared with the reported experimental spectroscopy. After resolving the signals, we successfully distinguished the reactive intermediates in a carbon dioxide reduction reaction, which provides an atomic-scale understanding of this important reaction.

Author contributions: T.C. and W.A.G. designed research; T.C. and A.F. performed research; T.C. and W.A.G. analyzed data; and T.C., A.F., and W.A.G. wrote the paper.

Reviewers: S.H.-S., Yale University; P.S., University of California, Los Angeles; and R.J.S., University of California, Berkeley.

The authors declare no conflict of interest.

Published under the PNAS license.

¹To whom correspondence should be addressed. Email: wag@caltech.edu.

This article contains supporting information online at www.pnas.org/lookup/suppl/doi:10.1073/pnas.1821709116/-DCSupplemental.

reducing CO₂ efficiently provides a means for both reducing the amount of CO₂ in the atmosphere from human activities and converting renewable energy (such as solar, wind, hydropower, etc.) into chemical forms, which facilitates the energy storage (3–7). CO₂RR to hydrocarbons is one of these promising solutions, which has been significantly advanced in the last 30 y (8–11) since the pioneering work of Hori et al. in 1985 (12). Copper (Cu) is the only single-metal electrocatalyst that produces significant amounts of hydrocarbons (3) and thus has been investigated extensively as a prototype for understanding the reaction mechanism both in experiment and in theory (8, 9, 13–22). Carbon monoxide (CO) is the first stable product from CO₂RR which can be further reduced to hydrocarbons (such as methane, ethylene, ethanol, etc.) at sufficiently negative potentials. Subtle changes (such as Cu facet, pH, the presence of oxygen, etc.) are observed to have a significant impact on the activity and selectivity for CO₂RR or CORR. Very recently, we found that water also participates in CORR via nonelectrochemical reactions, which further complicates the reaction network (23). To understand and explain these intriguing experimental observations, we need to predict and validate the fundamental reaction mechanism at the atomic scale.

Atomic-scale computational simulations have been applied extensively to investigate various aspects of CO₂RR and CORR on Cu (15, 16, 22), but many simulations did not include a realistic description of the solvent and applied potentials. Recently, we reported the reaction mechanism and kinetics with full explicit solvent and grand canonical QM simulations of the EEI to mimic operando experimental conditions (24). Using this unified framework, we systematically investigated the reaction mechanism of CO₂RR and CORR on Cu (100) to 12 kinds of hydrocarbons (25–27). To confirm the presence of these predicted reaction intermediates in operando experiments, we report here their fundamental vibrational density of states (*v*-DoSs) using operando quantum mechanics molecular dynamics (*o*-QM-MD) to closely simulate the operando experimental conditions, including the isotope shifts for ¹²C to ¹³C, ¹⁶O to ¹⁸O, and H to D, which sets the stage for experimental validation for the details of these *o*-QM-MD simulations. We are most interested in the long-lifetime reactive intermediates that may be observed experimentally, which provides a means of using the experiment to extract critical information about the reaction mechanism. With the key intermediates identified, experiments can then obtain detailed kinetic parameters providing a means for optimizing the kinetic processes.

The Performance of Perdew, Burke, and Ernzerhof Functional

To benchmark the performance of QM at the level of Perdew, Burke, and Ernzerhof (PBE) density functional theory (DFT), we calculated the vibrational frequencies of 14 isolated molecules (CH₄, C₂H₂, C₂H₄, C₂H₆, CH₂OH-CH₂OH, CH₃CH₂OH, CH₃CHO, CH₃COOH, CH₃OH, CHO-CH₂OH, CHO-CHO, H₂O, HCOOH, and CH₂=CHOH), the experimental data of which are available to compare with. As shown in *SI Appendix*, Fig. S1, *v*-QM predictions well reproduce the experimental frequencies with linear correlation of 1.0015 (shown in *SI Appendix*, Fig. S1). Thus, scaling factors are not necessary.

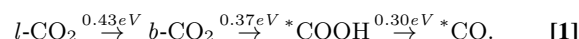
v-DoS from *o*-QM-MD

Vacuum QM (*v*-QM) has been extensively used in predicting the vibrational frequencies of intermediates at interface. However, we suspect that *v*-QM is not suitable for the EEI because the dynamics of the H₂O interacting with the reaction intermediates strongly affect the vibrational modes. In this work, we carried out explicit solvent calculation to simulate a water/Cu (100) interface and finely tuned the work function to match the experimentally applied voltage, as we did in our previous work (24). We further extended the *o*-QM-MD to 20 ps to produce a sufficiently long

trajectory as input of the two-phase thermodynamic (2PT) model (28) to generate the *v*-DoSs, which can be directly compared with operando experimental measurements. The details of the 2PT procedure for extracting the vibrational frequencies from *o*-QM-MD at 298 K are in *SI Appendix*. Using this framework, we systematically predicted the *v*-DoS of 22 intermediates from *o*-QM-MD (*SI Appendix*, Fig. S5). To compare, we also calculated the vibrational frequencies of these 22 intermediates from *v*-QM, in which the electrode was included and optimized, but without solvent or applied potential.

CO₂RR to CO

In our previous work, we predicted that the CO₂RR to CO involves physisorbed CO₂ (*l*-CO₂), chemisorbed CO₂ (*CO₂^{σ_c-} or *b*-CO₂), *COOH, and CO at pH 7 as follows (25):



The predicted *v*-DoSs from the 2PT analysis are shown in Fig. 1. The detailed results are as follows:

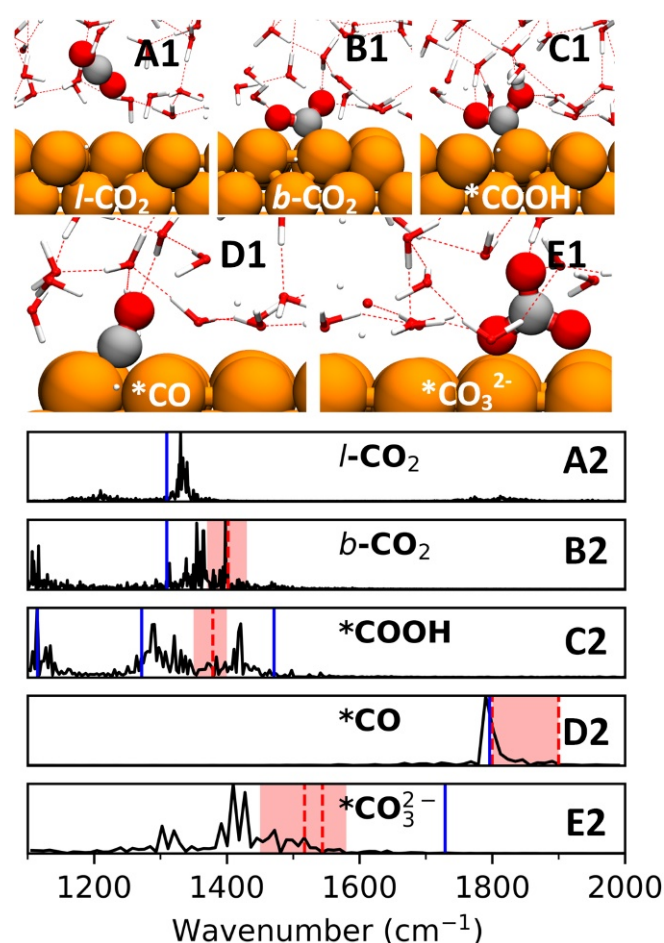


Fig. 1. Snapshots (A1–E1) of the structures and *v*-DoSs (A2–E2) of physisorbed CO₂ (*l*-CO₂), chemisorbed CO₂ (*b*-CO₂), *COOH, *CO, and *CO₃²⁻ from *o*-QM-MD simulations and 2PT analysis. In A1–E1, the color codes are Cu in orange, O in red, C in silver, and H in white. The hydrogen bonds are shown as dashed red lines. In A2–E2, *v*-DoS from *o*-QM-MD is shown as a solid black line, the experimental frequencies are shown as a red dashed line, and the vibrational frequencies from *v*-QM optimization are shown as solid blue lines for comparison. (*l*-CO₂ and *b*-CO₂ are the same from *v*-QM, because *b*-CO₂ is unstable in vacuum and automatically converts to *l*-CO₂ after optimization.)

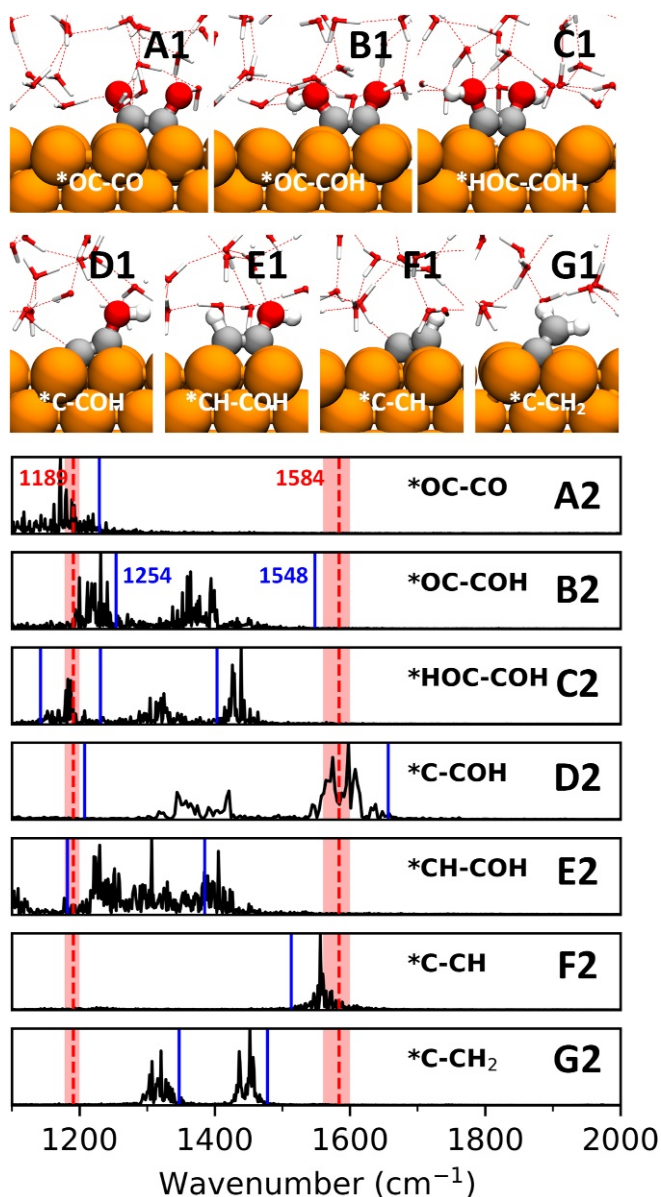


Fig. 2. Snapshots (A1–G1) and ν -DoSs (A2–G2) for $^*\text{OC-CO}$, $^*\text{OC-COH}$, $^*\text{HOC-COH}$, $^*\text{C-COH}$, $^*\text{CH-COH}$, $^*\text{C-CH}$, $^*\text{C-CH}_2$, and $^*\text{C=C=O}$. Notations are the same as in Fig. 1.

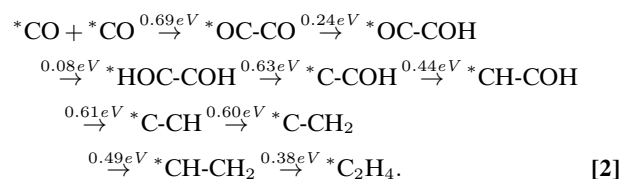
- For $l\text{-CO}_2$, the peak at $1,330\text{ cm}^{-1}$ is the O=C=O symmetrical stretch, which is IR inactive but Raman active.
- For $b\text{-CO}_2$, the peaks at $1,365\text{ cm}^{-1}$ and $1,397\text{ cm}^{-1}$ are the two C=O stretch modes from one C=O parallel and the other about 60° with the surface. The ν -QM of $l\text{-CO}_2$ and $b\text{-CO}_2$ are the same because $b\text{-CO}_2$ is unstable in vacuum and automatically converts to $l\text{-CO}_2$ after optimization.
- For $^*\text{COOH}$, the peak at $1,420\text{ cm}^{-1}$ is the C=O stretch, while $1,287\text{ cm}^{-1}$ is C-OH in-plane bend. Note that the ν -QM calculation gives symmetric and antisymmetric CO stretch at $1,248\text{ cm}^{-1}$ and $1,481\text{ cm}^{-1}$ but the hydrogen bonds (HBs) with H_2O lead to about 50 cm^{-1} redshifts of these two peaks.
- For $^*\text{CO}$, $1,790\text{ cm}^{-1}$ is C=O stretch of CO adsorbed on bridge sites. Instead, CO adsorbed on top sites leads to IR modes from $2,050\text{ cm}^{-1}$ to $2,100\text{ cm}^{-1}$ (29). The CO adsorbed on bridge sites has been observed but is considered inert to chemical reactions, thus having a longer lifetime (30).

- We assigned the surface-bounded $^*\text{CO}_3$ as carbonic acid based on the geometric features for ν -QM optimization. As shown in *SI Appendix, Table S1*, one C-O bond is significantly shorter (1.214 \AA) than the other two bonds (1.366 \AA), as expected for one C=O double bond and two C-O single bonds, which is also consistent with the frequency analysis shown in Fig. 1E2 and *SI Appendix, Fig. S5*: $1,720\text{ cm}^{-1}$ corresponds to C=O double-bond stretch and 986 cm^{-1} corresponds to C-O single-bond stretch. When this $^*\text{CO}_3$ is solvated in water with one Na^+ cation in o -QM-MD, the Bader charge analysis predicts a net charge of $-1.08 e^-$, close to -1 . However, after analyzing the bond distance of o -QM-MD, we found that the bond distances of C-O are 1.289 \AA , 1.311 \AA , and 1.312 \AA , significantly different from carbonic acid, but close to $^*\text{CO}_3^{2-}$ anions (shown in *SI Appendix, Table S1*). Because the Bader charge analysis is usually less reliable than the geometry analysis, at this negative applied potential we consider $^*\text{CO}_3$ as $^*\text{CO}_3^{2-}$ anions, although the carbonic form O=C=O_2^- may exist at positive potentials. This requires further study.

The spectroscopy of CO_2RR to CO has been extensively reported experimentally (20, 29–35). However, the assignments of the observed peaks remain controversial. We find that $b\text{-CO}_2$, $^*\text{COOH}$, and $^*\text{CO}_3^{2-}$ all exhibit comparable spectroscopy signals at $1,400\text{ cm}^{-1}$, making it difficult to distinguish them. According to the reaction mechanism (Eq. 1), at pH 7 the population of $b\text{-CO}_2$ is likely higher than that of $^*\text{COOH}$. Thus, we consider that the peaks observed at $1,400\text{ cm}^{-1}$ come from mostly $b\text{-CO}_2$ although $^*\text{CO}_3^{2-}$ is long lived and has signals at $1,400\text{ cm}^{-1}$. Because $^*\text{CO}_3^{2-}$ also has unique peaks at $1,034\text{ cm}^{-1}$ and $1,516\text{ cm}^{-1}$ (*SI Appendix, Fig. S5*), these peaks together could help to identify $^*\text{CO}_3^{2-}$ (35).

CORR to C_2H_4 and $\text{C}_2\text{H}_5\text{OH}$

The CORR has been studied more thoroughly because both the overall potential-determining step and the rate-determining step lie within the CORR. $\text{Cu}(100)$ is capable of reducing CO to ethylene (C_2H_4) at high pH. In our previous work, we predicted that the QM-based reaction mechanism at pH 7 and pH 12 involves at least eight intermediates as follows: (26)



The simulated ν -DoSs are shown in Fig. 2.

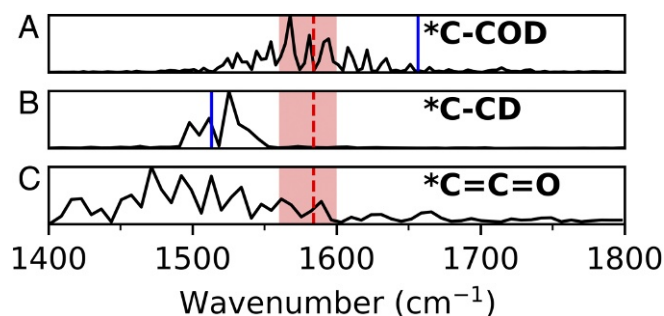


Fig. 3. ν -DoS of $^2\text{H(D)}$ -labeled (A) $^*\text{C-COD}$, (B) $^*\text{C-CD}$, and (C) $^*\text{C=C=O}$ in D_2O solvent. The frequencies of $^*\text{C=C=O}$ from ν -QM are $2,078\text{ cm}^{-1}$ and $1,211\text{ cm}^{-1}$ out of the range shown here ($1,400\text{--}1,800\text{ cm}^{-1}$).

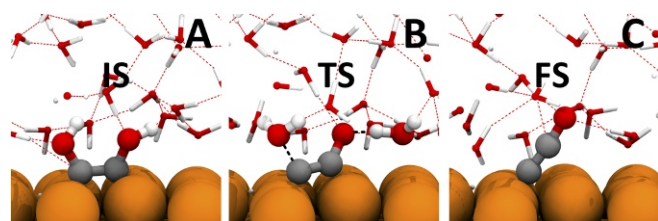


Fig. 4. (A–C) The snapshots of the initial state (IS, *HOC-COH) (A), the transition state (TS, *H₂O-C-CO-H₂O) (B), and the final state (FS, *C=C=O) (C) of reaction 3.

- For $^*\text{OC-CO}$, $1,171\text{ cm}^{-1}$ is from C-O^- stretch. Here, $v\text{-QM}$ gives symmetric and antisymmetric stretch at $1,039\text{ cm}^{-1}$ and $1,229\text{ cm}^{-1}$ but they are decoupled to $1,171\text{ cm}^{-1}$ in $o\text{-QM}$ -MD. Because the barrier is only 0.24 eV to the next species, this mode is unlikely to be observed.
- For $^*\text{OC-COH}$, $1,231\text{ cm}^{-1}$ is H-O-C in-plane bend, and the peaks around $1,360\text{ cm}^{-1}$ are from C=O stretch. Because the barrier is only 0.08 eV to the next species, this mode is unlikely to be observed.
- For $^*\text{HOC-COH}$, $1,439\text{ cm}^{-1}$ is from C=C stretch, $1,324\text{ cm}^{-1}$ is from H-O-C=C-O-H symmetric in-plane bend, and $1,187\text{ cm}^{-1}$ is from C-OH stretch. Since the barrier is 0.63 eV to the next step, these modes are likely to be observed.
- For $^*\text{C-COH}$, $1,609\text{ cm}^{-1}$ is from C=C stretch, which has the character of a C-C triple bond, because the barrier is 0.44 eV to the next step, these modes might be observed.
- For $^*\text{CH-COH}$, $1,422\text{ cm}^{-1}$ is from C=C stretch, and $1,251\text{ cm}^{-1}$ is from C-OH stretch. Because the barrier is 0.61 eV to the next step, these modes are likely to be observed.
- For $^*\text{C-CH}$, $1,559\text{ cm}^{-1}$ is from C=C stretch. Because the barrier is 0.60 eV to the next step, these modes are likely to be observed.
- For $^*\text{C-CH}_2$, both $1,451\text{ cm}^{-1}$ and $1,320\text{ cm}^{-1}$ are from C=C stretch. Because the barrier is 0.49 eV to the next step, these modes might not be observed.

At low potential in LiOH solutions, Pérez-Gallent et al. (20) experimentally distinguished two unique peaks, $1,191\text{ cm}^{-1}$ and $1,584\text{ cm}^{-1}$, and assigned $1,191\text{ cm}^{-1}$ as C-OH stretch of $^*\text{OC-COH}$. We find three early intermediates ($^*\text{OC-CO}$, $^*\text{OC-COH}$, and $^*\text{HOC-COH}$) with modes in this region but only $^*\text{HOC-COH}$ is predicted to be a long-lived species. Thus, we assign its mode at $1,189\text{ cm}^{-1}$ of $^*\text{HOC-COH}$ to the $1,191\text{ cm}^{-1}$ from the experiment.

The other peak at $1,584\text{ cm}^{-1}$ is more intriguing. Pérez-Gallent et al. (20) assigned this peak as the C=O stretch of $^*\text{OC-COH}$ based on a $v\text{-QM}$ calculation that predicted a peak at $1,576\text{ cm}^{-1}$. Indeed, in our $v\text{-QM}$ calculation we find this mode at $1,548\text{ cm}^{-1}$ (Fig. 2B2) too. However, with solvation and applied potential, this $1,548\text{ cm}^{-1}$ peak significantly redshifts to $1,360\text{ cm}^{-1}$, which is unlikely to explain the experiment. Instead, we find that $^*\text{C-COH}$ with a peak at $1,609\text{ cm}^{-1}$ and $^*\text{C-CH}$ with a peak at $1,559\text{ cm}^{-1}$ are more likely to explain the experimental peak at $1,584\text{ cm}^{-1}$. Both of these peaks correspond to a C-C triple bond interacting with the surface. Because the barrier out of $^*\text{C-CH}$ is 0.60 eV while that out of $^*\text{C-COH}$ is 0.44 eV , it may be that the observed line is dominated by the $^*\text{C-CH}$, but we expect that the $^*\text{C-COH}$ with a larger dipole might have a stronger intensity.

Isotope Simulations

The mode at $1,584\text{ cm}^{-1}$ can only be observed using D_2O solvent; otherwise, it is fully covered by a water O-H bending band (from $1,650\text{ cm}^{-1}$ to $1,450\text{ cm}^{-1}$). To directly compare with experiment, we carried out isotope simulations replacing all H

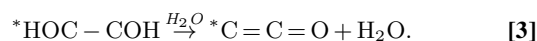
with D and calculated the v -DoSs of two possible candidates (*C-COD and *C-CD) as shown in Fig. 3. Both *C-COD and *C-CD exhibit about 25 cm^{-1} redshift due to the isotope effect, which leaves *C-COD as a better candidate to explain the experiment.

To provide the basis for definitive experimental validation we also report the isotope effects of ^{13}C and ^{18}O for these modes in *SI Appendix, Fig. S6*, which could serve a guidance for future isotope experiments.

Surface Ketene

Interestingly, we find that $^*\text{C}=\text{C}=\text{O}$ also exhibits signals in the $1,584\text{-cm}^{-1}$ region as shown in Fig. 3C. This is surprising because $v\text{-QM}$ predicts only two peaks at $1,211\text{ cm}^{-1}$ and $2,078\text{ cm}^{-1}$, which are from $\text{O}=\text{C}=\text{C}$ asymmetric and symmetric stretch, but the peaks at the $1,584\text{-cm}^{-1}$ range are absent. We attribute the emergence of $1,584\text{ cm}^{-1}$ of $^*\text{C}=\text{C}=\text{O}$ at the CORR condition for two reasons: First, $^*\text{C}=\text{C}=\text{O}$ is likely negative charged; and second, $^*\text{C}=\text{C}=\text{O}$ always interacts with water via HB, which weakens the $\text{C}=\text{O}$ double band, leaving $\text{C}=\text{C}$ sharing the triple-bond character similarly to $^*\text{C-COH}$, which is another case that shows the critical role of $o\text{-QM-MD}$ in predicting the operando experiment.

The presence of surface ketene ($^*C=O$) was first proposed by Calle-Vallejo and Koper (15). In our previous work, we found that $^*C=O$ is thermodynamically stable, but kinetically inhibited due to the high free-energy barrier (0.69 eV). Therefore, we previously excluded $^*C=O$ as a major intermediate. In this work, we found an additional pathway of $^*C=O$ formation from $^*HOC-COH$ via dehydration as follows:



The snapshots of the initial state, the transition state, and the final state are shown in Fig. 4. *o*-QM-MD free-energy calculations predicted the barrier to be 0.59 eV, which is similar to the other barriers involved in CORR. Thus, it is very possible that $\text{C}=\text{C}=\text{O}$ could present as a long-lived intermediate especially at low overpotential and high pH, in which condition nonelectrochemical reactions are promoted because the electrochemical reactions are suppressed.

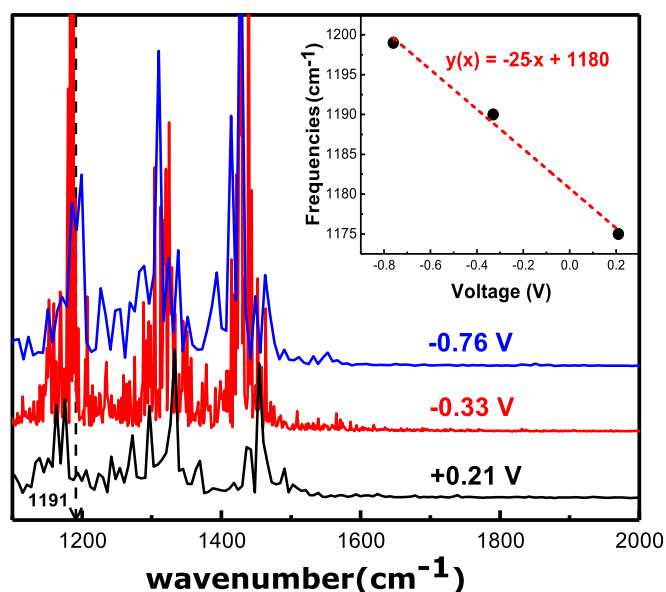


Fig. 5. The simulated potential-dependent *v*-DoSs of *HOC-COH at +0.21 V, -0.33 V, and -0.76 V. *Inset* shows the blue shift of the 1,191-cm⁻¹ peak (a feature of C-O stretch of C-OH) as a function of applied potential.

Stark Effect

Taking $^*\text{HOC-COH}$ as an example, we carried out simulations at +0.21 V, -0.33 V, and -0.76 V to investigate the electric field effect by removing one electron (+1 net charge), staying neutral, and adding one electron (-1 net charge). The predicted $v\text{-DoS}$ is shown in Fig. 5. As discussed above, we have distinguished the $1,191\text{ cm}^{-1}$ wavenumber as a feature of $^*\text{HCO-COH}$. We found this $1,191\text{ cm}^{-1}$ wavenumber undergoes a blue shift as applied potentials become more negative with a rate of about $25\text{ cm}^{-1}/\text{V}$, which reasonably agrees with experimental observations (20).

Summary

We carried out 20-ps $o\text{-QM-MD}$ simulations to determine the vibrational frequencies at 298 K to identify possible reactive intermediates in CO_2RR to CO and CORR to C_2H_4 while including an explicit solvent and the effect of the applied potential. We find significant differences in the vibrational frequency predictions between traditional $v\text{-QM}$ and $o\text{-QM-MD}$ for cases such as $^*\text{CO}_3$, $^*\text{OC-COH}$, and $^*\text{C=C=O}$. Thus, we recommend $o\text{-QM-MD}$ as a more reliable method to simulate and interpret the experimental spectroscopy at operando conditions.

From $o\text{-QM-MD}$ 2PT analysis, we assign the following: the experimental peak at $1,191\text{ cm}^{-1}$ to C-O stretch of $^*\text{HOC-COH}$, which is predicted at $1,189\text{ cm}^{-1}$ from $o\text{-QM-MD}$, and the

experimental peak at $1,584\text{ cm}^{-1}$ to C-C stretch of $^*\text{C-COD}$, which is predicted at $1,581\text{ cm}^{-1}$ from $o\text{-QM-MD}$.

Furthermore, we identified $^*\text{C=C=O}$, coming from an additional pathway of $^*\text{HOC-COH}$ dehydration, as another possible long-lived intermediate via a nonelectrochemical reaction, which likely explains the hydrocarbon formation [such as acetate (CH_3COO^-) and ethanol] at low overpotentials using oxygen-derived Cu nanoparticles (NPs) or Cu NPs with rich grain boundaries (9).

This combination of $o\text{-QM-MD}$ and experiment uses the best aspects of each: $o\text{-QM-MD}$ can predict the atomic structures but is limited in timescale, size scale, and accuracy. Instead, experiments can characterize the real system and provide signals produced by some intermediate, but have difficulties in resolving the atomic structure of reactive intermediates. Combining them fills the gap to provide the means of fully understanding the EEI and using this to design dramatically improved electrocatalytic processes.

ACKNOWLEDGMENTS. This work was supported by the Joint Center for Artificial Photosynthesis, a Department of Energy (DOE) Energy Innovation Hub, supported through the Office of Science of the US DOE under Award DE-SC0004993. These studies used the Extreme Science and Engineering Discovery Environment which is supported by National Science Foundation Grant ACI-1053575. This work is supported by Collaborative Innovation Center of Suzhou Nano Science & Technology, the Priority Academic Program Development of Jiangsu Higher Education Institutions (PAPD), the 111 Project.

1. Aresta M, Dibenedetto A, Angelini A (2014) Catalysis for the valorization of exhaust carbon: From CO_2 to chemicals, materials, and fuels. Technological use of CO_2 . *Chem Rev* 114:1709–1742.
2. Otto A, Grube T, Schiebahn S, Stolten D (2015) Closing the loop: Captured CO_2 as a feedstock in the chemical industry. *Energy Environ Sci* 8:3283–3297.
3. Hori Y (2008) Electrochemical CO_2 reduction on metal electrodes. *Modern Aspects of Electrochemistry*, eds Vayenas C, White R, Gamboa-Aldeco M (Springer, New York), Vol 42, pp 89–189.
4. Kortlever R, Shen J, Schouten KJP, Calle-Vallejo F, Koper MTM (2015) Catalysts and reaction pathways for the electrochemical reduction of carbon dioxide. *J Phys Chem Lett* 6:4073–4082.
5. Gattrell M, Gupta N, Co A (2006) A review of the aqueous electrochemical reduction of CO_2 to hydrocarbons at copper. *J Electroanal Chem* 594:1–19.
6. Kondratenko EV, Mul G, Baltrusaitis J, Larrazabal GO, Perez-Ramirez J (2013) Status and perspectives of CO_2 conversion into fuels and chemicals by catalytic, photocatalytic and electrocatalytic processes. *Energy Environ Sci* 6:3112–3135.
7. Schouten KJP, Calle-Vallejo F, Koper MTM (2014) A step closer to the electrochemical production of liquid fuels. *Angew Chem Int Ed* 53:10858–10860.
8. Liu M, et al. (2016) Enhanced electrocatalytic CO_2 reduction via field-induced reagent concentration. *Nature* 537:382–386.
9. Li CW, Ciston J, Kanan MW (2014) Electroreduction of carbon monoxide to liquid fuel on oxide-derived nanocrystalline copper. *Nature* 508:504–507.
10. Dinh CT, et al. (2018) CO_2 electroreduction to ethylene via hydroxide-mediated copper catalysis at an abrupt interface. *Science* 360:783–787.
11. Mariano RG, McKelvey K, White HS, Kanan MW (2017) Selective increase in CO_2 electroreduction activity at grain-boundary surface terminations. *Science* 358:1187–1192.
12. Hori Y, Kikuchi K, Suzuki S (1985) Production of CO and CH_4 in electrochemical reduction of CO_2 at metal electrodes in aqueous hydrogen carbonate solution. *Chem Lett* 14:1695–1698.
13. Kuhl KP, Cave ER, Abram DN, Jaramillo TF (2012) New insights into the electrochemical reduction of carbon dioxide on metallic copper surfaces. *Energy Environ Sci* 5:7050–7059.
14. Schouten KJP, Qin Z, Gallent EP, Koper MTM (2012) Two pathways for the formation of ethylene in CO reduction on single-crystal copper electrodes. *J Am Chem Soc* 134:9864–9867.
15. Calle-Vallejo F, Koper MTM (2013) Theoretical considerations on the electroreduction of CO to C_2 species on Cu(100) electrodes. *Angew Chem* 52:7282–7285.
16. Nie X, Esopi MR, Janik MJ, Asthagiri A (2013) Selectivity of CO_2 reduction on copper electrodes: The role of the kinetics of elementary steps. *Angew Chem* 52:2459–2462.
17. Schouten KJP, Pérez Gallent E, Koper MTM (2014) The influence of pH on the reduction of CO and to hydrocarbons on copper electrodes. *J Electroanal Chem* 716:53–57.
18. Montoya JH, Shi C, Chan K, Nørskov JK (2015) Theoretical insights into a CO dimerization mechanism in CO_2 electroreduction. *J Phys Chem Lett* 6:2032–2037.
19. Verdager-Casadevall A, et al. (2015) Probing the active surface sites for CO reduction on oxide-derived copper electrocatalysts. *J Am Chem Soc* 137:9808–9811.
20. Pérez-Gallent E, Figueiredo MC, Calle-Vallejo F, Koper MTM (2017) Spectroscopic observation of a hydrogenated CO dimer intermediate during CO reduction on Cu(100) electrodes. *Angew Chem* 56:3621–3624.
21. Garza AJ, Bell AT, Head-Gordon M (2018) Mechanism of CO_2 reduction at copper surfaces: Pathways to C_2 products. *ACS Catal* 8:1490–1499.
22. Peterson AA, Abild-Pedersen F, Studt F, Rossmeisl J, Nørskov JK (2010) How copper catalyzes the electroreduction of carbon dioxide into hydrocarbon fuels. *Energy Environ Sci* 3:1311–1315.
23. Lum Y, Cheng T, Goddard WA, Ager JW (2018) Electrochemical CO reduction builds solvent water into oxygenate products. *J Am Chem Soc* 140:9337–9340.
24. Cheng T, Wang L, Merinov BV, Goddard WA (2018) Explanation of dramatic pH-dependence of hydrogen binding on noble metal electrode: Greatly weakened water adsorption at high pH. *J Am Chem Soc* 140:7787–7790.
25. Cheng T, Xiao H, Goddard WA (2016) Reaction mechanisms for the electrochemical reduction of CO_2 to CO and formate on the Cu(100) surface at 298 K from quantum mechanics free energy calculations with explicit water. *J Am Chem Soc* 138:13802–13805.
26. Cheng T, Xiao H, Goddard WA (2017) Full atomistic reaction mechanism with kinetics for CO reduction on Cu(100) from ab initio molecular dynamics free-energy calculations at 298 K. *Proc Natl Acad Sci USA* 114:1795–1800.
27. Cheng T, Xiao H, Goddard WA (2017) Nature of the active sites for CO reduction on copper nanoparticles; suggestions for optimizing performance. *J Am Chem Soc* 139:11642–11645.
28. Lin ST, Maiti PK, Goddard WA (2010) Two-phase thermodynamic model for efficient and accurate absolute entropy of water from molecular dynamics simulations. *J Phys Chem B* 114:8191–8198.
29. Heyes J, Dunwell M, Xu B (2016) CO_2 reduction on Cu at low overpotentials with surface-enhanced in situ spectroscopy. *J Phys Chem C* 120:17334–17341.
30. Gunathunge CM, Ovalle VJ, Li Y, Janik MJ, Waegle MM (2018) Existence of an electrochemically inert CO population on Cu electrodes in alkaline pH. *ACS Catal* 8:7507–7516.
31. Figueiredo MC, Ledezma-Yanez I, Koper MTM (2016) In situ spectroscopic study of CO_2 electroreduction at copper electrodes in acetonitrile. *ACS Catal* 6:2382–2392.
32. Pérez-Gallent E, Marcandalli G, Figueiredo MC, Calle-Vallejo F, Koper MTM (2017) Structure- and potential-dependent cation effects on CO reduction at copper single-crystal electrodes. *J Am Chem Soc* 139:16412–16419.
33. Zhu S, Jiang B, Cai WB, Shao M (2017) Direct observation on reaction intermediates and the role of bicarbonate anions in CO_2 electrochemical reduction reaction on Cu surfaces. *J Am Chem Soc* 139:15664–15667.
34. Gunathunge CM, et al. (2017) Spectroscopic observation of reversible surface reconstruction of copper electrodes under CO_2 reduction. *J Phys Chem C* 121:12337–12344.
35. Chernyshova IV, Somasundaran P, Ponnurangam S (2018) On the origin of the elusive first intermediate of CO_2 electroreduction. *Proc Natl Acad Sci USA* 115:E9261–E9270.